

# Full-field X-ray reflection microscopy of epitaxial thin-films

Nouamane Laanait,<sup>a\*</sup> Zhan Zhang,<sup>b</sup> Christian M. Schlepütz,<sup>b</sup> Joan Vila-Comamala,<sup>b</sup> Matthew J. Highland<sup>c</sup> and Paul Fenter<sup>a\*</sup>

<sup>a</sup>Chemical Sciences and Engineering Division, Argonne National Laboratory, Argonne, IL 60439, USA, <sup>b</sup>X-ray Science Division, Argonne National Laboratory, Argonne, IL 60439, USA, and <sup>c</sup>Materials Science Division, Argonne National Laboratory, Argonne, IL 60439, USA.

\*E-mail: nlaanait@anl.gov, fenter@anl.gov

Novel X-ray imaging of structural domains in a ferroelectric epitaxial thin film using diffraction contrast is presented. The full-field hard X-ray microscope uses the surface scattering signal, in a reflectivity or diffraction experiment, to spatially resolve the local structure with 70 nm lateral spatial resolution and sub-nanometer height sensitivity. Sub-second X-ray exposures can be used to acquire a 14  $\mu\text{m} \times 14 \mu\text{m}$  image with an effective pixel size of 20 nm on the sample. The optical configuration and various engineering considerations that are necessary to achieve optimal imaging resolution and contrast in this type of microscopy are discussed.

**Keywords:** X-ray surface diffraction; X-ray microscopy; interfaces and thin films; materials science.

© 2014 International Union of Crystallography

## 1. Introduction

X-ray techniques, such as diffraction and crystallography, excel at characterizing the structure of a multitude of systems across the physical sciences, in a variety of complex environments (Kaufmann, 2012), often with sub-Å spatial resolution. The measured structure, however, represents a statistical average over all the configurations present in a system, within the sampling volume of the X-ray beam size. This limits the utility of traditional X-ray scattering techniques in the study of systems whose properties are inherently linked to structural heterogeneity. To address the need for local structural information at the nano and mesoscopic scales, the capabilities of X-ray imaging have grown tremendously over the past two decades (Chapman *et al.*, 2013; Miao *et al.*, 1999; Robinson *et al.*, 2001; Thibault *et al.*, 2008; Fenter *et al.*, 2006a). This progress has been made possible by the emergence of X-ray sources with improved spatial coherence (Reich, 2013) and the substantial advances in X-ray optics (Ice *et al.*, 2011; Mimura *et al.*, 2010; Yan *et al.*, 2013).

X-ray imaging of local structures and their dynamics should contribute immensely to our understanding of numerous condensed-matter systems. Hard X-rays interact weakly with matter, enabling ease of operation in complex environments for *in situ* characterization of samples. One area of interest is in epitaxial thin films whose behavior is strongly coupled to the lattice (Spaldin *et al.*, 2010). X-ray microscopy can be used to study the local evolution of order parameters in these systems, as a function of extreme thermodynamic potentials (*e.g.* high temperatures and magnetic

fields). These physical conditions are often incompatible with probe microscopies but are routinely accessible in hard X-ray diffraction experiments (Fong *et al.*, 2004). Another advantage of X-rays is their small scattering cross section, which in most practical situations allows for a direct and quantitative interpretation of data within the framework of first-order perturbation in scattering theory (Als-Nielsen & McMorrow, 2011). Yet, X-rays are notoriously difficult to focus (Als-Nielsen & McMorrow, 2011), imposing severe constraints on the fabrication of optical elements and their performance, and limiting the throughput of any hard X-ray imaging system. These factors have hampered the development of X-ray microscopy compared with electron microscopy (Urban, 2009), for which lenses with large numerical apertures are far more accessible.

The development of X-ray interfacial microscopy, with high depth penetration capability, structural and elemental sensitivity, and simple quantitative interpretation, is motivated by the need to understand complex interfacial phenomena ranging from the recent observation of collective behavior at buried interfaces of complex oxides thin films (Hwang *et al.*, 2012) to the reactions at buried solid–liquid interfaces at extreme temperature and under aggressive chemical conditions (Teng *et al.*, 2001). The main challenge of X-ray interfacial microscopy is its use of the weak surface scattering signal that is orders of magnitude smaller than the scattering from a bulk crystal. This technique, therefore, requires not only high-efficiency optics but also high mechanical stability in its instrumentation, to ensure the positional stability of the sample during long X-ray exposures.

Several X-ray techniques image extended systems with interfacial sensitivity (Holt *et al.*, 2013). They mainly employ a scanning probe configuration, where a focused beam is rastered across the sample and the diffraction signal is imaged in the far-field. The spatial resolution that these scanning probes achieve is limited by the focus size, of the order of tens of nanometers. The resolution can be further improved by implementing a coherent imaging technique known as ptychography (Hruszkewycz *et al.*, 2013; Godard *et al.*, 2011; Dierolf *et al.*, 2010), in principle, achieving diffraction-limited imaging with nanometer resolution. The continued development of these imaging techniques, with the increased coherence of X-ray sources and further refinement of image reconstruction algorithms (Zhang *et al.*, 2013), will substantially advance our understanding of the static structure of interfacial systems. However, the real-time monitoring of the structural response of epitaxial thin films is greatly facilitated by the development of full-field interfacial microscopy. This capability will be most useful in studies where the relevant length scales range from tens to hundreds of nanometers as resolved by current imaging optics. Furthermore, the time evolution of the local structure can be acquired in real time (*i.e.* in a stroboscopic mode).

In this article we present the imaging of the local structure of interfaces and thin films using a full-field hard X-ray microscope. The new capabilities of the X-ray reflection interface microscope (XRIM) are demonstrated by resolving the domain configurations in an epitaxial ferroelectric thin film with 70 nm lateral resolution, acquiring a  $14\ \mu\text{m} \times 14\ \mu\text{m}$  image with sub-second temporal resolution. A complete description of the design, implementation and use of XRIM are also presented to highlight the engineering challenges of this technique and the opportunities it presents in characterizing the properties of heterogeneous materials.

## 2. X-ray reflection microscopy: a primer

### 2.1. Concept

The optical configuration of XRIM is illustrated in Fig. 1 and consists of a condenser to illuminate the sample, and an objective lens to image the exit wavefield. Surface sensitivity is achieved in XRIM by using interface-specific scattering signals. Its implementation was only recently made possible by the availability of third-generation synchrotron X-ray sources with high flux and brilliance, as well as the increase in efficiency of hard X-ray optics. Fenter and co-workers were the first to demonstrate the surface sensitivity of a full-field microscope by imaging sub-nanometer high surface topography of a single crystal (Fenter *et al.*, 2006a, 2008). These initial investi-

gations demonstrated the sensitivity to surface structures that could be achieved by X-ray reflection microscopy, and highlighted the need for significant improvements in the design of the instrument to improve its resolution and optical throughput. Moreover, new contrast mechanisms, such as the diffraction contrast we use in §5, remained to be explored and applied to the imaging of thin films.

The optical configuration of XRIM is similar to the more widely available transmission X-ray microscopes (TXMs) that lack sensitivity to the interfacial structure (Schmahl *et al.*, 1980). XRIM differs from TXM in its ability to use scattered X-rays, instead of the transmitted beam, to image a structure. The condenser illuminates the sample with a beam whose divergence, ideally, matches the angular acceptance (numerical aperture) of the objective lens. The image that is projected on the camera has a lateral resolution that is inversely proportional to the numerical aperture of the objective lens. Technical details pertinent to the design, operation and performance of the microscope are presented in subsequent sections (§3 and §4).

### 2.2. Spatially resolved structure factor

XRIM images surfaces and interfaces by spatially resolving the interface-specific scattering intensity in direct space, with an image contrast that is controlled by the scattering vector,  $\mathbf{Q}$ . This technique is a conceptually simple extension of surface scattering. In a typical surface diffraction experiment [see Robinson & Tweet (1992) for a review], the intensity,  $I$ , is recorded as a function of the scattering transfer vector  $\mathbf{Q} = \mathbf{k}_{\text{out}} - \mathbf{k}_{\text{in}}$ , where  $\mathbf{k}_{\text{out}}$  is the outgoing (scattered) wavevector and  $\mathbf{k}_{\text{in}}$  is the incoming wavevector of the incident beam (see inset to Fig. 1). Within the kinematic approximation, the intensity is given by  $I \propto r_e^2 I_0 |F(\mathbf{Q})|^2$ , where  $r_e = 2.818 \times 10^{-5}\ \text{\AA}$  is the Thomson scattering length,  $I_0$  is the incident beam intensity and  $F(\mathbf{Q})$  is the (elastic) structure factor (*i.e.* the Fourier transform of the electron density). The fact that X-ray scattering is weak can be directly seen from the  $r_e^2$  term that

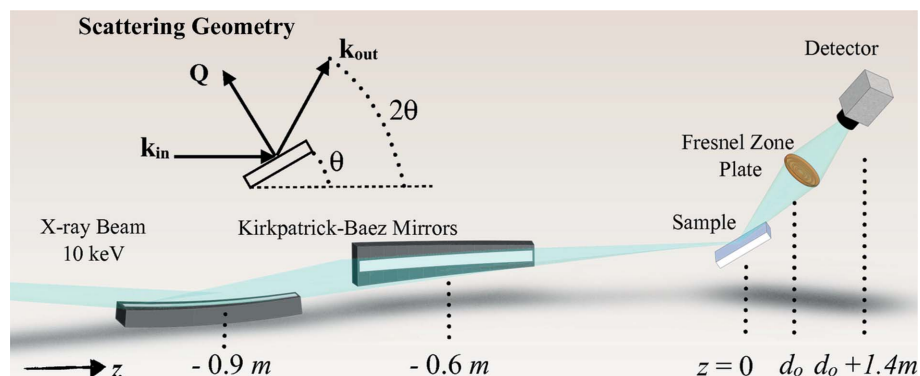


**Figure 1** Illustration of the optical configuration of XRIM (distances and components not drawn to scale). All distances are in the X-ray beam frame of reference. The object–lens distance,  $d_o \simeq 50\ \text{mm}$ , satisfies the lens equation and is determined by the focal length of the Fresnel zone plate with an outermost zone width of 60 nm ( $f = 48\ \text{mm}$ ). Inset: specular diffraction geometry indicating sample rotation angle ( $\theta$ ), lens/detector rotation angle ( $2\theta$ ) and scattering vector  $\mathbf{Q}$ .

enters the intensity. The structure factor can be decomposed to explicitly include the contribution of the bulk crystal and the interface, as follows,

$$F = F_{uc} F_{CTR} + F_{INT}, \quad (1)$$

where  $F_{uc}$  refers to the unit-cell form factor of the crystal substrate,  $F_{CTR}$  to the crystal truncation rod form factor (Robinson, 1986) and  $F_{INT}$  is the interfacial structure factor, including all surface layers with properties that differ from those of the bulk crystal (including any substrate layers that are structurally relaxed due to the presence of the interface and any deposited material such as a thin film) (Fenter, 2002). Interfacial scattering is typically performed under scattering conditions that do not satisfy the bulk Laue condition  $\mathbf{Q} = \mathbf{G}$ , where  $\mathbf{G} = [(2\pi/a)H, (2\pi/b)K, (2\pi/c)L]$  represents the set of reciprocal lattice vectors of the substrate's unit cell, and where the Bragg indices,  $H$ ,  $K$  and  $L$ , are integers. Instead, the interfacial Laue condition is determined by integer indices  $H$  and  $K$  defined by the two-dimensional surface lattice and  $L$  is continuous along the surface normal direction. Therefore, the modulus square of the interfacial structure factor is not significantly large, and, combined with the small scattering length, produces weak scattering intensities in the range  $(10^{-5}-10^{-8}) \times I_0$ .

In conventional surface diffraction, the measured intensity  $I$  is the *total* response of all the scattering centers in the region illuminated by the beam and the derived structure is averaged over all configurations (Fenter & Zhang, 2005; Yacoby *et al.*, 2002; Björck, 2011). The XRIM spatially resolves the lateral distribution of the scattering intensity by magnifying the scattered wave ( $\mathbf{k}_{out}$ ) after it exits the object's surface. This instrument therefore records the spatially resolved scattering intensity,  $I(x, y; \mathbf{Q})$ , where  $(x, y)$  denotes the position of an effective pixel on the sample surface, whose size is determined by the magnification of the microscope (as defined in §4). The characteristics of the image (*e.g.* contrast and signal strength) are determined by the specific scattering condition ( $\mathbf{Q}$ ) as demonstrated in §5. Hence, the optimal imaging conditions are normally defined by a traditional surface diffraction measurement in which a preliminary understanding of the various factors in equation (1) can be obtained. A pixel-by-pixel analysis of the intensity in the image should allow, in principle, the determination of a spatially resolved structure factor and consequently the local structure. In this article, the presented examples of XRIM exclusively use specular surface diffraction, where  $H = K = 0$  and  $L \neq 0$ . Henceforth, the obtained imaging contrast is only sensitive to the electron density profile along the surface normal.

### 3. Microscope design

The new capabilities of the microscope in the investigation of the local structure of thin films such as ferroelectrics are enabled by the substantial advances in the design and performance of the instrument. In comparison with the first-generation instrument (Fenter *et al.*, 2006a), an order of magnitude reduction in exposure time and more than a

twofold increase in resolution were achieved. These advances are discussed here.

#### 3.1. Optical configuration

The XRIM instrument is located at station 33 (ID-D) of the Advanced Photon Source at Argonne National Laboratory (see Fig. 2). The X-ray source size (FWHM) is 780 and 50  $\mu\text{m}$ , with divergence (FWHM) of 35 and 17  $\mu\text{rad}$ , in the horizontal and vertical directions, respectively. A double-bounce Si(111) single-crystal monochromator (liquid-nitrogen-cooled) at 45 m from the source selects a photon energy of 10 keV, producing a beam with a flux of  $10^{13}$  photons  $\text{s}^{-1}$  and an energy bandwidth  $\Delta E/E = 3 \times 10^{-4}$ . This energy represents an optimal choice, considering the efficiency of the microscope optics, the attenuation of X-rays by propagation from the monochromator to the sample, including the sample environments, then to the detector. The monochromator also focuses the beam in the sagittal plane to match the horizontal size of the beam with the optical aperture of the microscope condenser. No other optical elements were placed between the monochromator and the condenser.

The intrinsically weak surface diffraction signals, typically in the range  $(10^{-5}-10^{-8}) \times I_0$ , necessitate the use of a condenser optic that produces a high flux density (flux/illumination area). Various optical elements were tested as condenser optics, including a Fresnel zone plate (Xradia Corporation), a tapered single-bounce monocabillary (Xradia Corporation) and a pair of Kirkpatrick–Baez mirrors (KB) (Kirkpatrick & Baez, 1948) (see Fig. 1). The KB mirrors produce an illumination field at the beam focal spot (sample position) of approximately  $10 \mu\text{m} \times 10 \mu\text{m}$  (FWHM, horizontal  $\times$  vertical) with a flux of  $4 \times 10^{12}$  photons  $\text{s}^{-1}$ . This was roughly ten times

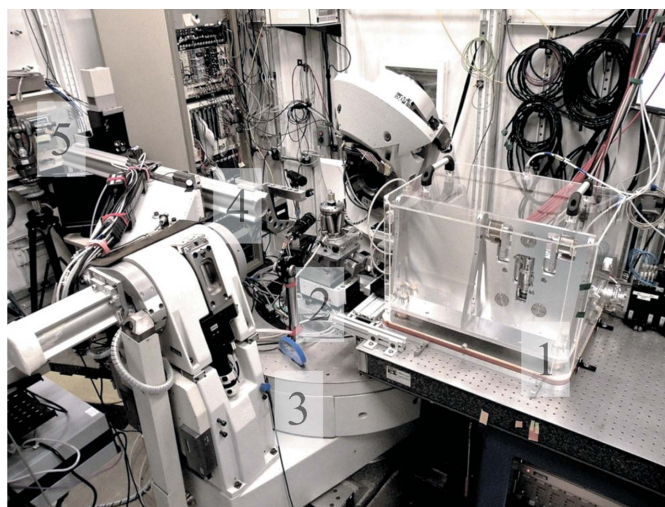


**Figure 2** Photograph of the X-ray reflection microscope setup at station 33 (ID-D) of the Advanced Photon Source. From right to left, in the direction of X-ray beam propagation: (1) Kirkpatrick–Baez mirror system, (2) sample stage on (3) the Kappa Newport diffractometer, (4) objective lens stage and (5) detector on the detector arm of the diffractometer (shown at  $2\theta = 0$ ).

higher than the flux density achieved with either a Fresnel zone plate or an X-ray capillary (the former with both a lower focused beam flux and similar focused beam cross section; the latter with a similar focused beam flux but a lower flux density). The order of magnitude increase in flux density translates into a reduction of the image acquisition time by the same amount.

The KB mirrors, consisting of rhodium-coated Si slabs, are equipped with asymmetric benders to dynamically adjust their curvature (Instrument Design Technologies). The length of the mirrors ( $l$ ) along the beam is 280 mm  $\times$  200 mm (horizontal mirror  $\times$  vertical mirror). A glancing angle  $\alpha$  of 5–6 mrad is typically used to maximize the efficiency of the condenser and to match the numerical aperture (NA) of the objective lens. The nominal beam divergence produced by the mirrors,  $\delta_{\text{KB}} = 2\text{NA} = \text{OA}/w$ , is determined by the optical aperture  $\text{OA} = l\alpha$ , and the working distance  $w$ , where  $w = 0.6$  m (vertical) and  $w = 0.89$  m (horizontal). The X-ray beam size at the sample is monitored with a custom X-ray eye composed of a scintillator, a lens and an optical camera. The effective pixel size of 0.65  $\mu\text{m}$  of the X-ray eye is sufficient to resolve the focused beam spot size of 10  $\mu\text{m}$   $\times$  10  $\mu\text{m}$ . The divergence of the beam is verified from a separate measurement of the beam size at a distance of 1400 mm downstream from the sample position using the XRIM X-ray camera (see below).

The beam divergence is tuned in the range 1.5–2 mrad by changing the glancing angle of the KB mirror,  $\alpha$ , to match the numerical aperture of the objective lens being used. One advantage of using a KB pair as condenser is the ability to dynamically adjust the size and divergence of the illumination, thereby controlling the field of view and the resolution; however, the accessible range in the current system is limited since the mirror's working distance is fixed.

The focused beam is deflected by an angle of  $2\alpha$  from its initial propagation direction in both the horizontal and the vertical directions. The sample stage, the objective lens stage and the detector all reside on a six-circle Kappa diffractometer (Newport Corporation) (see Fig. 2) that share a common rotational center. The entire diffractometer is translated and rotated both laterally and vertically (*i.e.* two translations + two rotations) so that the incident beam intersects the rotational center of the diffractometer. Incidentally, this ensures that the optical axis of the objective lens is collinear with the propagation direction of the focused X-ray beam. Finer adjustments of the objective lens consisting of pitch and yaw rotations in the plane normal to the optical axis are also performed to eliminate off-axis aberrations in the imaging (Born & Wolf, 1980).

The objective lens is a Fresnel phase zone plate (FZP). Multiple FZPs were used in the results reported here, with their outermost zone widths ranging from 60 to 80 nm, and an outer diameter of 100  $\mu\text{m}$ . The FZPs were manufactured at the Center of Nanoscale Materials at Argonne National Laboratory combining high-resolution e-beam lithography and gold electrodeposition (Gorelick *et al.*, 2010); their first-order diffraction efficiency at 10 keV is approximately 5%. The

FZPs are mounted on an XYZ stage (VP-25XA-XYZL; Newport Corporation) with high-precision positioning and minimal thermally induced drift. Surface imaging imposes stringent constraints on the holding stability of the objective lens and sample stages. In particular, the combination of the small surface scattering cross section and the low efficiency of the objective FZP can demand continuous exposures of 10–100 s to obtain an image with good signal-to-noise ratio. The lens is initially placed at a distance from the sample that satisfies the thin-lens equation, and the position is finely tuned by imaging a test pattern in transmission geometry using absorption contrast. During the operation of the microscope in TXM mode, the illumination field is also imaged at the focal plane, where the sample is eventually placed, to obtain a more accurate characterization of the beam size than is feasible with the direct imaging discussed above. Images of the illumination field also serve to map the efficiency of the detector's active area.

The XRIM detector system (Xradia Corporation) consists of a scintillator that converts X-rays to visible light, followed by an aberration-corrected optical lens (Nikon Plan Fluor, multi-immersion, NA = 0.75) with a 20 $\times$  magnification. A mirror reflector, placed at 45 $^\circ$  from the optical axis, directs the optical beam to a motorized tube lens, and then onto a 1 Megapixel optical charge-coupled device (CCD) (model C4742-98, Hamamatsu Photonics) with a pixel size of 13  $\mu\text{m}$ . The overall magnification of the microscope,  $M = M_{\text{opt}}M_{\text{X-ray}}$ , is the product of optical magnification ( $M_{\text{opt}} = 20$ ) and magnification by the Fresnel zone plate,  $M_{\text{X-ray}} = (d_i - f)/f$ , where  $d_i$  is the image–FZP distance and  $f$  is the focal length of the lens. For instance,  $f = 48.4$  mm for a 60 nm outermost zone width FZP, giving an overall magnification  $M \simeq 560$ , which corresponds to an effective pixel size of 23 nm at the sample surface. In Bragg geometry, the effective pixel size within the scattering plane (*i.e.* the vertical direction in the present images) is enlarged by a factor that is a function of the detector's viewing angles. For specular reflection (see inset to Fig. 1), where the angle of incidence is equal to the exit angle, this factor is given by  $1/\sin(\theta)$ , where  $\theta$  is the angle of incidence of the X-ray beam with respect to the sample surface.

The optical magnification of the detector is adjustable by changing the optical lens. During alignment of the instrument with a direct or scattered beam, a 2 $\times$  magnifying lens is used, so that the angular acceptance of the camera is approximately three times larger than the size of the illuminating beam in the far-field (at the detector position). The alignment of the FZP, by positioning in the plane normal to the beam, is also performed with a 2 $\times$  optical magnification. Due to its low efficiency, the FZP transmits most of the beam, refocusing only a small portion of it to form an image that is projected on top of the transmitted beam. To eliminate this intensely bright background from the image, a central beam stop consisting of a gold wire (200  $\mu\text{m}$  thick) is inserted vertically into the path of the beam prior to the condenser and positioned to absorb all photons from the center of the beam. This beam stop creates a dark-field region in the camera where the FZP projects the image.

### 3.2. Diffractometer configuration

Surface diffraction measurements require multiple sample and detector rotational degrees of freedom to reach a scattering condition,  $\mathbf{Q}$ . Generally, a diffractometer provides access to all necessary rotations and ensures that they share a common rotational center. We have found, however, that mechanical vibrations at the sample position with displacement amplitudes as high as 70 nm in the 10–60 Hz range caused severe blurring of the images. Although these mechanical vibrations originate in the experimental hutch floor, the Kappa diffractometer is highly compliant in this frequency range. Therefore a primary consideration in the current implementation of XRIM was to mechanically decouple the sample stage (and its degrees of freedom) from the diffractometer to reduce the impact of these instabilities on the observed images.

The use of a standalone sample stage improved the performance of the instrument. The stage is mounted on the same base where the diffractometer sits but is mechanically separated from the detector rotation stages. This newly designed sample stage is an assembly of three stages providing eight degrees of freedom (five rotations and three translations), as shown in Fig. 3. The motor stage assembly consists of a one-circle segment ( $\theta$ ), a one-circle goniometer ( $\varphi$ ) (both from Huber Diffractionstechnik) and a hexapod (M810, Physik Instrumente). The one-circle  $\theta$  segment is mounted at an offset angle of  $11^\circ$ , thereby resulting in an angular range of the stage of  $-4^\circ$  to  $26^\circ$ , and providing access to a maximum vertical momentum transfer of  $4.5 \text{ \AA}^{-1}$  at 10 keV. The

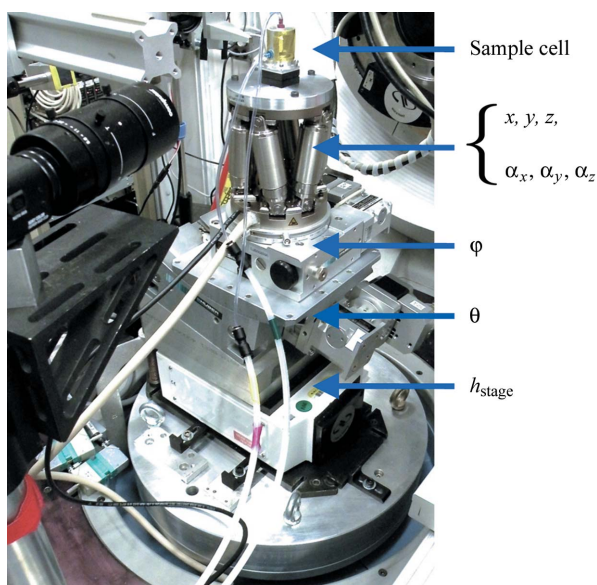


**Figure 3** Photograph of the sample stage and the available degrees of freedom of the sample. The hexapod performs three translations ( $x, y, z$ ) and rotations about those axes ( $\alpha_{x,y,z}$ ) for sample alignment. The  $\varphi$ -stage rotates the sample about the surface normal. The incidence angle on the sample is controlled by the  $\theta$ -stage. The entire height of the assembly is adjusted with  $h_{\text{stage}}$  so that the rotation center of the  $\theta$ -stage coincides with the rotation center of the diffractometer. For scale, the sample cell is two inches high.

hexapod has three translations and three rotations that are used primarily for sample alignment, and the frame of reference of these motions is adjustable, as well as a motorized height adjustment. This design was chosen to meet existing constraints of the diffractometer, mainly its fixed rotation center (placing a strict limit on the height of the assembly), and to minimize the number of mounting points so that the configuration is as rigid as possible. It is particularly important that the sample and detector rotations coincide so that instrument motions in reciprocal space illuminate the same physical region on the sample (see Fig. 3). The main disadvantage of the hexapod is its positional drift when exposed to minute temperature gradients (measured at  $0.3 \mu\text{m min}^{-1}$ ). This drift is reduced (to  $\sim 30 \text{ nm min}^{-1}$ ) once the stage is thermally equilibrated. No active vibration isolation of the sample stage was used, in part due to spatial constraints, but also because rotations of the sample stage, to change the scattering condition, are accompanied by large shifts in the assembly's center of mass. A vibration analysis confirmed that the largest vibrational amplitude at the sample is 20 nm (independent of the rotational angle).

The objective lens stage and the detector are mounted on the detector arm of the Kappa diffractometer, as shown in Fig. 2. The detector arm can rotate both within the vertical scattering plane ( $2\theta$ ) (up and down in Fig. 2) as well as in the out-of-plane direction ( $\nu$ ) (left and right in Fig. 2). To illustrate how the sample stage and detector arm rotations are used, we restrict our attention to specular surface diffraction. At the specular condition (see inset to Fig. 1), the only non-zero component of the scattering vector is  $\mathbf{Q} = Q\mathbf{n}$ , where  $\mathbf{n}$  is the surface normal, and its magnitude is given by  $Q = 4\pi/\lambda \sin(2\theta/2)$ , where  $\lambda$  is the wavelength of the X-ray beam. Different values of the scattering vector are accessed through changes in  $\theta$  and  $2\theta$ . To reach off-specular scattering conditions, sample rotations about the surface normal  $\varphi$  and detector motions in the out-of-plane direction  $\nu$  must be performed, and will not be described here [for instance, see Schlepütz *et al.* (2011)].

A deficiency in the current implementation of the XRIM system resides in the vibration instabilities in the diffractometer detector arm, which are amplified when  $2\theta \gg 0^\circ$ . We observe that the FZP stage can reach vibrational amplitudes as high as 40 nm, blurring the images and coarsening the observed resolution of the microscope (see §4.1). Future XRIM designs will decouple the objective lens stage from the detector arm, to separately satisfy the high stability requirements of the objective lens and the significant mechanical requirements of the X-ray camera.

## 4. Microscope operation and performance

### 4.1. Image processing

Microscopy of interfacial systems is challenged by their intrinsically weak signals. Where possible, long exposures are avoided to minimize the effect of drift on the image quality. Instead, a series of images are taken with short acquisition

times at identical sample position and scattering condition. The detector exposure time is chosen so that the images have a sufficiently large signal-to-noise ratio (typically 2:1 ratio). Image registration is then performed on the full image series with standard techniques such as cross-correlation at sub-pixel resolution that repositions subsequent images with respect to the first exposure (Zitova & Flusser, 2003). This permits image averaging with good signal-to-noise ratio. Under scattering conditions where the intensities are weak, image registration methods that are based on intensity correlation measures (*e.g.* cross-correlation) do not perform well. Instead, more sophisticated feature detection algorithms, such as scale-invariant feature transforms (Lowe, 2004), are needed. All image acquisition and processing were performed in *ImageJ* (Schneider *et al.*, 2012) using homemade or open-source plugins (Schindelin *et al.*, 2012).

Additional steps are taken to remove extrinsic contributions to the images. As discussed previously in §2 and demonstrated in §5, the XRIM signal and image contrast are fully quantitative and incorporate important intrinsic information that any image processing should preserve. The extrinsic backgrounds (*i.e.* the ‘read’ signal and ‘dark’ counts inherent to each image scaled by the exposure time) are subtracted from the raw image (Fenter *et al.*, 2006*b*). An additional flat-field correction to the images is necessary because of the intensity variation within the illumination

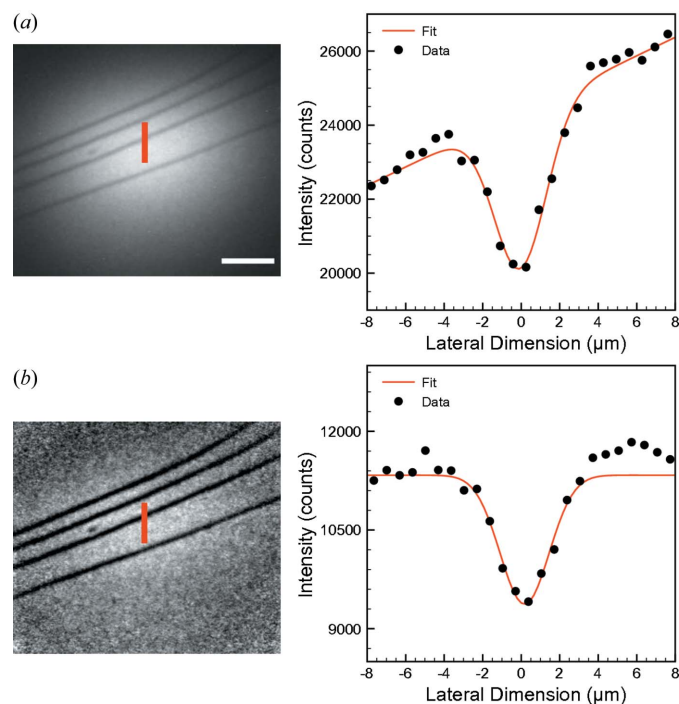


**Figure 4**

Flat-field correction of an XRIM image. (a) Raw image of crystallographic steps on the (001) surface of a  $\text{KAlSi}_3\text{O}_8$  single crystal acquired at  $Q \simeq 0.5 \text{ \AA}^{-1}$ . The scale bar is  $2.5 \mu\text{m}$ . (b) Flat-field-corrected image. In both images the vertical (red) line marks the location of the line profiles. The contrast is defined by  $C = (I_{\text{step}} - I_b) / I_b$ , where  $I_b$  is the background intensity and  $I_{\text{step}}$  is the intensity at the step (dip). These values are determined by fitting a Gaussian function plus a linear background to the profiles. A contrast of  $-0.18 \pm 0.01$  is found in (a) and  $-0.17 \pm 0.03$  in (b).

region. Previously we have addressed this by scanning the condenser FZP to create a uniformly illuminated region, but this is not possible using the KB mirrors as a condenser. Another approach is to acquire a ‘flat-field’ image of the illumination that can be used to normalize any image. This can be obtained in transmission geometry by moving the sample out of the beam, but this is not feasible in the Bragg reflection geometry that we utilize for interfacial imaging. Moreover, the illumination function can change with the scattering condition. It is therefore necessary to normalize images without a measured flat-field image [see Russ (2011) for instance].

To achieve a proper flat-field correction, we employ a combination of morphological filters and a Gaussian blur filter to extract an illumination function from the raw image. The ‘bottom-hat’ transform is used to remove all features from the raw image replacing them with their mean bright value. Any remaining features in the flat-field image have weak contrast and are removed with a Gaussian blur filter. The radius of the Gaussian blur filter is kept at a minimum (10–20 pixels) to extract an illumination function as close as possible to the one in the raw image. The original unfiltered raw image is then divided by the illumination function. This procedure was applied to an image of  $0.64 \text{ nm}$ -high crystallographic steps on the (001) surface of a  $\text{KAlSi}_3\text{O}_8$  (orthoclase) single crystal (Fig. 4). The visibility of steps in the image is enhanced with the removal of the illumination function, but the local contrast in the unfiltered data remains unchanged, as confirmed by line profiles taken at the same pixel positions on the images (Fig. 5).

## 4.2. Spatial resolution

The nominal resolution of the microscope was tested by resolving  $60 \text{ nm}$ -wide gold nanostructures while operating in a transmission geometry (TXM) (image not shown). A more relevant characterization of the XRIM resolution is obtained by imaging domain boundaries in a thin film of  $\text{PbTiO}_3$  on  $\text{SrTiO}_3$  (001)-oriented single-crystal substrate. These domain boundaries, as discussed in §5, do not scatter the X-ray beam

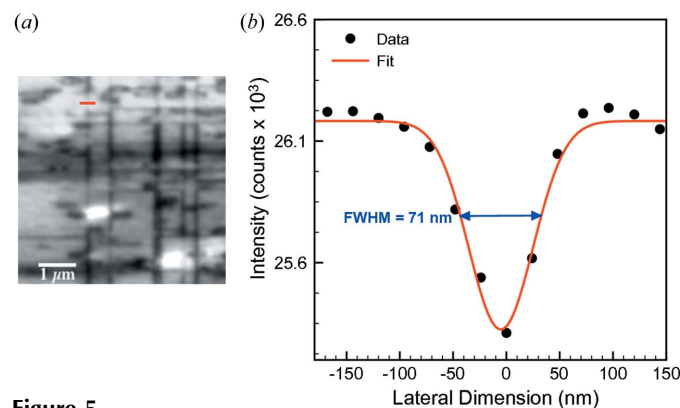


**Figure 5**

Characterization of the microscope lateral resolution in reflection geometry. (a) Structural domains in a ferroelectric thin film collected at  $Q_{002} = 3.06 \text{ \AA}^{-1}$ . The scale bar is  $1 \mu\text{m}$  and the horizontal (red) line indicates where the line profile shown in (b) is extracted. The fit to the data is a combination of a Gaussian function and a linear background.

along the specular direction. Consequently, they exhibit dark contrast when imaged at the  $\text{PbTiO}_3$  002 Bragg condition. An image of the  $\text{PbTiO}_3$  film is shown in Fig. 5(a). A line profile across the domain boundary is taken along the  $x$ -direction of the image (Fig. 5b), to avoid the  $1/\sin(\theta)$  distortion introduced in the image's  $y$ -direction at this incidence angle ( $\theta \approx 17^\circ$ ). A lateral resolution of 71 nm is found from the full width at half-maximum of the Gaussian function fitted to the profile (see Fig. 5b). The good contrast and signal-to-noise ratio of the image provides a rigorous measurement of the resolution.

In the above resolution characterization, the effective pixel size at the sample location is 23 nm and the Fresnel zone plate has a 60 nm outermost zone width. Therefore, the lateral resolution should be at least 60 nm. The coarsening of the resolution in surface imaging is expected, chiefly, from the mechanical instabilities present in the system (§4) in terms of higher vibration amplitudes at non-zero detector angles. The coarsening of the microscope resolution when operated in Bragg geometry highlights the severe demands of mechanical stability that this imaging technique imposes on a diffractometer. Nevertheless, the 70 nm resolution that is now routinely accessible with the current instrument is a significant improvement over the previous implementation, which achieved a 180 nm lateral resolution.

### 5. Ferroelastic and ferroelectric domains in a thin film

The XRIM system finds a natural application in structural studies of epitaxially grown ferroelectrics on single-crystal substrates. The use of thin-film diffraction and other forms of phase contrast makes XRIM a powerful approach to image the various structural domains present in these systems, as demonstrated in this section.

Ferroelectric materials such as  $\text{PbTiO}_3$  have a net switchable polarization vector below a critical temperature  $T_c$  (Rabe *et al.*, 2007). In a displacive ferroelectric, the polarization is a result of a distortion in the unit cell during the structural phase transition from a paraelectric cubic phase to a ferroelectric tetragonal. In the ferroelectric phase and under compressive strain,  $\text{PbTiO}_3$  primarily forms ferroelectric domains ( $c$ -domains) with a polarization vector along the [001] ( $c$ -axis) of the  $\text{SrTiO}_3$  substrate (see Fig. 6a). In sufficiently thick  $\text{PbTiO}_3$  films the drive for strain relaxation can enable the formation of ferroelastic  $90^\circ$  domains ( $a$ -domains) in the film, with an in-plane polarization vector pointing in one of the four symmetry-equivalent directions, *i.e.* {100} [see Lee & Baik (2006) for a review and references therein]. Domain walls along the {101} planes separate regions of the film with a polarization vector that are perpendicular to each other and form a coherent boundary between  $c$ -domains and  $a$ -domains (see Fig. 6a). The domain configurations present in a ferroelectric film will depend on the electrostatic and elastic boundary conditions, as well as the growth conditions. The commonly observed configuration is the poly twin domain structure formed by  $c$ -domains and  $a$ -domains, known as  $c/a/c/a$  (Koukhar *et al.*, 2001). These various polarization states

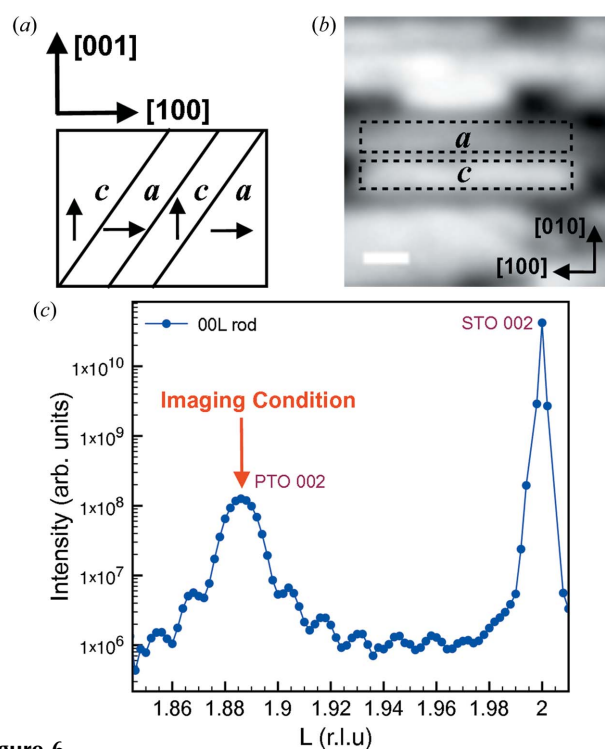


**Figure 6** Imaging of ferroelectric and ferroelastic domains in  $\text{PbTiO}_3$ . (a) Illustration of the domain structures present in a ferroelectric thin film. The arrows indicate the direction of the polarization vector with respect to the crystallographic directions of the cubic substrate  $\text{SrTiO}_3$  (001). (b) XRIM image showing a sequence of  $a$ - and  $c$ -domains, acquired at 002 reflection of  $\text{PbTiO}_3$ . The scale bar is 300 nm. The crystallographic axes in the image indicate the measured orientation of the lattice, determined by  $\text{SrTiO}_3$  101 and 011 reflections. (c) Specular truncation rod measured from the  $\text{PbTiO}_3/\text{SrTiO}_3$  system. The arrow points to the scattering condition (PTO 002) where the XRIM imaging was performed.

lead to a modification of the local atomic structure that XRIM can resolve.

The system that we study consists of a 30 nm-thick  $\text{PbTiO}_3$  film on  $\text{SrTiO}_3$  (001)-oriented single-crystal substrate. The film was grown by metal-organic chemical vapor deposition under conditions similar to those previously described (Stephenson *et al.*, 2003). The thickness of the film and its lattice constants ( $c = 4.145 \text{ \AA}$  and  $a = b = 3.897 \text{ \AA}$ ) were determined by standard crystal truncation rod measurements, specifically the 00L (shown in Fig. 6c) and 10L rod (data not shown).

To probe the different domain configurations in the film, the  $\text{PbTiO}_3$  002 diffraction was used for all the images presented here, as shown in Fig. 6(c). The X-ray imaging contrast at  $\mathbf{Q}_{002}$  is sensitive to many structural features in the film (see Figs. 6 and 7), such as thickness variations of the  $c$ -domains,  $c/a$  domain walls and  $a$ -domains. At the film's specular Bragg reflection, all bright contrast is due to  $c$ -domains; their  $d$ -spacing satisfies the Bragg condition, causing all the layers of the film to scatter X-rays in-phase. A sequence of  $a$ - and  $c$ -domains are shown in Fig. 6(b), surrounded by  $c/a$  domain walls (discussed below). It is noteworthy to emphasize that the crystallographic axes that label the XRIM images (Figs. 6 and 7) are the measured orientation of the substrate's lattice as determined from the 101 and 011 reflections.

The imaging of an  $a$ -domain using diffraction contrast at  $\mathbf{Q}_{002}$  is indirect; as can be clearly seen from Fig. 6(a), the  $\text{PbTiO}_3$  002 reflection always carries an intensity contribution from the strong diffraction of neighboring  $c$ -domains. Consequently, the intensity at the location of an  $a$ -domain will be weaker (by approximately 10–15%) compared with the intensity at the location of a  $c$ -domain. For direct imaging and higher contrast of the  $a$ -domains, the scattering vector must be tuned to their diffraction peaks which are accessible at off-specular conditions; for instance, the [100] oriented domains scatters at ( $H \simeq \pm 0.12$ ,  $K = 0$ ,  $L \simeq 2$ ) referenced with respect to  $\text{SrTiO}_3$ 's reciprocal lattice (Kwak *et al.*, 1994; Lee & Baik, 1999). The imaging of these domains revealed the existence of two  $a$ -domain variants with different  $d$ -spacing and will be reported elsewhere.

The three main structural features which XRIM is most sensitive at the  $\text{PbTiO}_3$  002 reflection are shown and labelled in Fig. 7. Region 1 shows a  $c$ -domain. As the Bragg condition is satisfied by the  $c$ -domains, the contrast in the image is sensitive to variations in their structure throughout the *entire* thickness

of the film, *i.e.* 30 nm. For instance, the intensity follows the scaling law  $I(\mathbf{Q}_{002}) \simeq N^2$ , where  $N$  is the number of film layers. Therefore, variations in the intensity within region 1 are the product of local thickness variations in this particular  $c$ -domain. A rough estimate of this thickness variation ( $\sim 4$  nm) is obtained, once we use the average thickness ( $\sim 30$  nm) measured by surface X-ray diffraction and assume that the substrate's contribution to the intensity at this scattering condition is negligible.

The second general feature are the  $c/a$  domain walls, indicated by arrows 2 and 3. At the surface of the film, a height displacement  $\delta z \simeq 1.2$  nm between the  $a$ - and  $c$ -domains occurs due to the tetragonal crystal structure (Nagarajan *et al.*, 2002). This shift in height at the  $c/a$  domain wall causes a phase shift of the X-rays by  $Q\delta z$  and leads to destructive interference at the location of this boundary (dark contrast). The two in-plane orientations of the  $c/a$  walls follow from the crystallographic cubic symmetry of the substrate. The variation in contrast of different  $c/a$  boundaries in the film may be related to the variations in the  $d$ -spacing of the  $a$ -domains mentioned earlier. Additional work is needed to quantitatively address these findings.

## 6. Conclusion

We have reported on the first demonstration of full-field X-ray microscopy of ferroelectric thin films using diffraction contrast. The microscope reveals rich and spatially complex domain configurations in this particular thin film that future studies will explore in more detail. The X-ray imaging of both ferroelectric domains, ferroelastic domains and their coherent boundaries with 70 nm lateral resolution and sub-nanometer high sensitivity represents a substantial addition to the imaging tools that are currently available to characterize ferroelectrics and other thin films. Furthermore, the direct interpretation of the contrast and the formation of a  $14 \mu\text{m} \times 14 \mu\text{m}$  image with sub-second resolution presents us with the opportunity to study the real-time structural evolution of thin films as a function of external fields. The demonstrated real-time imaging, where exposures as short as 200 ms can be used, will allow the study of the evolution of domain configurations in a ferroelectric thin film as a function of external fields (Nelson *et al.*, 2011; Kalinin *et al.*, 2010), accessing at least an order of magnitude faster polarization switching dynamics than current piezoforce microscopes. The depth penetration of hard X-rays, of the order of micrometers, should also facilitate the *in operando* imaging of thin films in complex device architectures that are not easily accessible by probe-based microscopies.

We have also presented the design and operation of the full-field hard X-ray microscope. The results demonstrate the need to fully decouple the sample and the detector motions. This is necessary to eliminate the propagation of mechanical instabilities and to allow the vibration isolation of the sample and the objective lens from the typically noisy experimental floor of a synchrotron facility. Decoupling of the objective lens stage from the detector arm will be performed in future

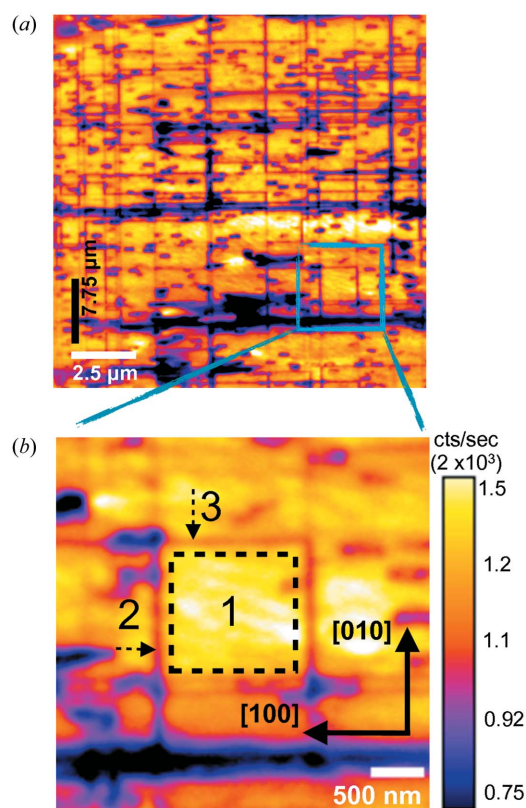


**Figure 7**

Full-field image of domain configurations in  $\text{PbTiO}_3$ . (a) XRIM image acquired at the 002 reflection of  $\text{PbTiO}_3$ . The image is the average of six 0.5 s exposures after registration and flat-field correction (see §4). The horizontal scale bar is  $2.5 \mu\text{m}$ , and the vertical scale bar is  $7.75 \mu\text{m}$  due to the projection discussed in §3. (b) A close-up view of the boxed region in (a). The color bar refers to the number of detector counts per second and the scale bar is  $500 \text{ nm}$ . The image uses  $146 \times 146$  pixels, with an effective pixel size of  $23 \text{ nm}$ . Region 1:  $c$ -domain with a polarization vector along [001]. Arrows 2 and 3 point to  $c/a$  domain boundaries in the film along the two principal crystallographic axes, [010] and [100], respectively.

implementations to achieve higher spatial resolutions. Moreover, time-resolved diffraction studies in a pump–probe configuration, routinely performed at synchrotron sources with sub-nanosecond resolution, could be simply implemented in the full-field diffraction microscope with minimal change in the setup of the latter (Do *et al.*, 2004).

The exquisite sensitivity of XRIM to a variety of heterogeneous local structures illustrates the versatility of this technique and highlights its potentially broad applicability to mesoscale investigations of condensed matter systems, and characterizations studies in materials science.

We would like to acknowledge Jonathan Tischler (X-ray Science Division, Argonne National Laboratory) for his invaluable advice and suggestions during the design of the microscope. We also would like to thank Peter Eng (CARS, University of Chicago) for installing and configuring the Kirkpatrick–Baez mirror system. We have benefited from many discussions with Steve Wang (Washington State University) and Dillon Fong (Argonne National Laboratory). We thank Zunping Liu (X-ray Science Division, Argonne National Laboratory) for assistance with the hutch vibration measurements. This work was supported by the Geosciences Research Program of the Office of Basic Energy Sciences, US Department of Energy (DOE), through Contract number DE-AC02-06CH11357 at Argonne National Laboratory, and through a collaborative ‘Partner User Proposal’ awarded for the development of this instrument. The X-ray data were collected at the X-ray Operations and Research beamline 33-ID-D at the Advanced Photon Source, Argonne National Laboratory. MJH was supported by US DOE, Office of Basic Energy Sciences, Materials Sciences and Engineering Division. The submitted manuscript has been created by UChicago Argonne, LLC, Operator of Argonne National Laboratory (‘Argonne’). Argonne, a US Department of Energy Office of Science laboratory, is operated under Contract number DE-AC02-06CH11357. The US Government retains for itself, and others acting on its behalf, a paid-up non-exclusive irrevocable worldwide license in said article to reproduce, prepare derivative works, distribute copies to the public, and perform publicly and display publicly, by or on behalf of the Government.

## References

Als-Nielsen, J. & McMorrow, D. (2011). *Elements of Modern X-ray Physics*, 2nd ed. Hoboken: John Wiley and Sons.

Björck, M. (2011). *J. Appl. Cryst.* **44**, 1198–1204.

Born, M. & Wolf, E. (1980). *Principles of Optics*, 6th ed. Oxford: Pergamon Press.

Chapman, H., Kirz, J. & Stampanoni, M. (2013). *Synchrotron Radiat. News*, **26**, 2–3.

Dierolf, M., Menzel, A., Thibault, P., Schneider, P., Kewish, C. M., Wepf, R., Bunk, O. & Pfeiffer, F. (2010). *Nature (London)*, **467**, 436–439.

Do, D. H., Evans, P. G., Isaacs, E. D., Kim, D. M., Eom, C. B. & Dufresne, E. M. (2004). *Nat. Mater.* **3**, 365–369.

Fenter, P. (2002). *Rev. Mineral. Geochem.* **49**, 149–220.

Fenter, P., Catalano, J. G., Park, C. & Zhang, Z. (2006*b*). *J. Synchrotron Rad.* **13**, 293–303.

Fenter, P., Park, C., Kohli, V. & Zhang, Z. (2008). *J. Synchrotron Rad.* **15**, 558–571.

Fenter, P., Park, C., Zhang, Z. & Wang, S. (2006*a*). *Nat. Phys.* **2**, 700–704.

Fenter, P. & Zhang, Z. (2005). *Phys. Rev. B*, **72**, 081401.

Fong, D. D., Stephenson, G. B., Streiffer, S. K., Eastman, J. A., Auciello, O., Fuoss, P. H. & Thompson, C. (2004). *Science*, **304**, 1650–1653.

Godard, P., Carbone, G., Allain, M., Mastropietro, F., Chen, G., Capello, L., Diaz, A., Metzger, T., Stangl, J. & Chamard, V. (2011). *Nat. Commun.* **2**, 568.

Gorelick, S., Guzenko, V. A., Vila-Comamala, J. & David, C. (2010). *Nanotechnology*, **21**, 295303.

Holt, M., Harder, R., Winarski, R. & Rose, V. (2013). *Annu. Rev. Mater. Sci.* **43**, 183–211.

Hruszkewycz, S. O., Highland, M. J., Holt, M. V., Kim, D., Folkman, C. M., Thompson, C., Tripathi, A., Stephenson, G. B., Hong, S. & Fuoss, P. H. (2013). *Phys. Rev. Lett.* **110**, 177601.

Hwang, H. Y., Iwasa, Y., Kawasaki, M., Keimer, B., Nagaosa, N. & Tokura, Y. (2012). *Nat. Mater.* **11**, 103–113.

Ice, G. E., Budai, J. D. & Pang, J. W. (2011). *Science*, **334**, 1234–1239.

Kalinin, S. V., Morozovska, A. N., Chen, L. Q. & Rodriguez, B. J. (2010). *Rep. Prog. Phys.* **73**, 056502.

Kaufmann, E. N. (2012). *Characterization of Materials*, 2nd ed. New York: John Wiley and Sons.

Kirkpatrick, P. & Baez, A. V. (1948). *J. Opt. Soc. Am.* **38**, 766–774.

Koukhar, V., Pertsev, N. & Waser, R. (2001). *Phys. Rev. B*, **64**, 214103.

Kwak, B. S., Erbil, A., Budai, J. D., Chisholm, M. F., Boatner, L. A. & Wilkens, B. J. (1994). *Phys. Rev. B*, **49**, 14865.

Lee, K. & Baik, S. (2006). *Annu. Rev. Mater. Res.* **36**, 81–116.

Lee, K. S. & Baik, S. (1999). *J. Appl. Phys.* **85**, 1995.

Lowe, D. G. (2004). *Int. J. Comput. Vis.* **2**, 91–110.

Miao, J., Charalambous, P., Kirz, J. & Sayre, D. (1999). *Nature (London)*, **400**, 342.

Mimura, H. *et al.* (2010). *Nat. Phys.* **6**, 146.

Nagarajan, V., Roytburd, A., Stanishevsky, A., Prasertchoung, S., Zhao, T., Chen, L., Melngailis, J., Auciello, O. & Ramesh, R. (2002). *Nat. Mater.* **2**, 43.

Nelson, C. T., Gao, P., Jokisaari, J. R., Heikes, C., Adamo, C., Melville, A., Baek, S. H., Folkman, C. M., Winchester, B., Gu, Y., Liu, Y., Zhang, K., Wang, E., Li, J., Chen, L. Q., Eom, C. B., Schlom, D. G. & Pan, X. (2011). *Science*, **334**, 968–971.

Rabe, K. M., Ahn, C. H. & Triscone, J.-M. (2007). *Physics of Ferroelectrics*, Vol. 105 of *Topics in Applied Physics*, 1st ed. Berlin: Springer.

Reich, E. S. (2013). *Nature (London)*, **501**, 148–149.

Robinson, I. K. (1986). *Phys. Rev. B*, **33**, 3830–3836.

Robinson, I. K. & Tweet, D. J. (1992). *Rep. Prog. Phys.* **55**, 599.

Robinson, I. K., Vartanyants, I. A., Williams, G. J., Pfeifer, M. A. & Pitney, J. A. (2001). *Phys. Rev. Lett.* **87**, 195505.

Russ, J. C. (2011). *The Image Processing Handbook*, 6th ed. Boca Raton: CRC Press.

Schindelin, J., Arganda-Carreras, I., Frise, E., Kaynig, V., Longair, M., Pietzsch, T., Preibisch, S., Rueden, C., Saalfeld, S., Schmid, B., Tinevez, J. Y., White, D. J., Hartenstein, V., Eliceiri, K., Tomancak, P. & Cardona, A. (2012). *Nat. Methods*, **9**, 676–682.

Schleppütz, C. M., Mariager, S. O., Pauli, S. A., Feidenhans'l, R. & Willmott, P. R. (2011). *J. Appl. Cryst.* **44**, 73–83.

Schmahl, G., Rudolph, D., Niemann, B. & Christ, O. (1980). *Q. Rev. Biophys.* **3**, 297–315.

Schneider, C. A., Rasband, W. S. & Eliceiri, K. W. (2012). *Nat. Methods*, **9**, 671–675.

- Spaldin, N. A., Cheong, S.-W. & Ramesh, R. (2010). *Phys. Today*, **63**(10), 38–43.
- Stephenson, G., Fong, D., Murty, M. R., Streiffer, S., Eastman, J., Auciello, O., Fuoss, P., Munkholm, A., Aanerud, M. & Thompson, C. (2003). *Physica B*, **336**, 81–89.
- Teng, H. H., Fenter, P., Cheng, L. & Sturchio, N. C. (2001). *Geochim. Cosmochim. Acta*, **65**, 3459–3474.
- Thibault, P., Dierolf, M., Menzel, A., Bunk, O., David, C. & Pfeiffer, F. (2008). *Science*, **321**, 379–382.
- Urban, K. W. (2009). *Nat. Mater.* **8**, 260–262.
- Yacoby, Y., Sowwan, M., Stern, E., Cross, J. O., Brewes, D., Pindak, R., Pitney, J., Dufresne, E. M. & Clarke, R. (2002). *Nat. Mater.* **1**, 99–101.
- Yan, H., Chu, Y. S., Maser, J., Nazaretski, E., Kim, J., Kang, H. C., Lombardo, J. J. & Chiu, W. K. S. (2013). *Sci. Rep.* **3**, 1307.
- Zhang, F., Peterson, I., Vila-Comamala, J., Diaz, A., Berenguer, F., Bean, R., Chen, B., Menzel, A., Robinson, I. K. & Rodenburg, J. M. (2013). *Opt. Express*, **21**, 13592–13606.
- Zitova, B. & Flusser, J. (2003). *Image Vis. Comput.* **21**, 977–1000.